Journal of Hydrology 571 (2019) 593–604

Contents lists available at ScienceDirect

Journal of Hydrology

journal homepage: www.elsevier.com/locate/jhydrol

Research papers

Long-term flood-hazard modeling for coastal areas using InSAR measurements and a hydrodynamic model: The case study of Lingang New City, Shanghai

Jie Yin[a,b,c], Qing Zhao[a,b,*], Dapeng Yu[d], Ning Lin[e], Julia Kubanek[f], Guanyu Ma[a,b], Min Liu[a,b,c], Antonio Pepe[g]

[a] Key Laboratory of Geographic Information Science (Ministry of Education), East China Normal University, China
[b] School of Geographic Sciences, East China Normal University, China
[c] Institute of Eco-Chongming, East China Normal University, China
[d] Centre for Hydrological and Ecosystem Science, Department of Geography, Loughborough University, UK
[e] Department of Civil and Environmental Engineering, Princeton University, USA
[f] Department of Earth and Planetary Sciences, McGill University, Canada
[g] Institute for Electromagnetic Sensing of the Environment (IREA), National Research Council (CNR) of Italy, Italy

ARTICLE INFO

This manuscript was handled by Geoff Syme, Editor-in-Chief, with the assistance of Ashok Mishra, Associate Editor

Keywords:
Coastal flooding
Sea level rise
Land subsidence
InSAR
FloodMap

ABSTRACT

In this paper, we study long-term coastal flood risk of Lingang New City, Shanghai, considering 100- and 1000-year coastal flood return periods, local seal-level rise projections, and long-term ground subsidence projections. TanDEM-X satellite data acquired in 2012 were used to generate a high-resolution topography map, and multi-sensor InSAR displacement time-series were used to obtain ground deformation rates between 2007 and 2017. Both data sets were then used to project ground deformation rates for the 2030s and 2050s. A 2-D flood inundation model (FloodMap-Inertial) was employed to predict coastal flood inundation for both scenarios. The results suggest that the sea-level rise, along with land subsidence, could result in minor but non-linear impacts on coastal inundation over time. The flood risk will primarily be determined by future exposure and vulnerability of population and property in the floodplain. Although the flood risk estimates show some uncertainties, particularly for long-term predictions, the methodology presented here could be applied to other coastal areas where sea level rise and land subsidence are evolving in the context of climate change and urbanization.

1. Introduction

The global mean sea-level has risen at an average rate of 1.6–1.9 mm/year during the 20th century (Hay et al., 2015), and the rate is projected to accelerate, with a total sea-level rise (SLR) of up to 2 m over the 21st century (Oppenheimer and Alley, 2016). However, the projections remain quite uncertain due to difficulties in estimating the rate of melting of glaciers and the melting of the Greenland and Antarctic ice sheets. The fifth Assessment Report (AR5) of the Intergovernmental Panel on Climate Change (IPCC) suggests higher SLR rates throughout this century based on recent ice-sheet observations (IPCC, 2014), hence increased flooding risks for low-lying coastal zones. Coastal inundation risks under sea-level rise have been assessed and mapped extensively for many coastal regions, including, e.g., in Charlestown, RI, USA (Grilli et al., 2017), in the Italian coastal plains (Antonioli et al., 2017), in the coastal zones of Poland (Paprotny and Terefenko, 2017), in southeast Queensland, USA (Mills et al., 2016), in New York, USA (Orton et al., 2015, Lin and Shullman, 2017), and in Shanghai in China (Wang et al., 2012).

Moreover, non-climate-related anthropogenic processes, such as ground subsidence due to groundwater extraction, extensive coastal settlements in lands reclaimed from the sea, and complex subsidence phenomena related to artificial sea walls, will exacerbate the flooding risk of coastal zones. There is a global consensus that land subsidence is a major problem in low-lying coastal zones around the world (Jelgersma, 1996; Ericson et al., 2006; Syvitski et al., 2009; Teatini et al., 2011). Local sinking of land resulting from anthropogenic and natural processes, in combination with sea level rise caused by climate change, makes the situation worse for coastal settlements. A large number of studies has already stressed the significance of relative SLR in increasing coastal flood frequency and intensity (Karegar et al., 2017; Little et al., 2016; Shi et al., 2012; Cayan et al., 2008; Carminati and

* Corresponding author.
E-mail address: qzhao@geo.ecnu.edu.cn (Q. Zhao).

https://doi.org/10.1016/j.jhydrol.2019.02.015
Received 25 August 2018; Received in revised form 16 January 2019; Accepted 7 February 2019
Available online 15 February 2019
0022-1694/ © 2019 Elsevier B.V. All rights reserved.

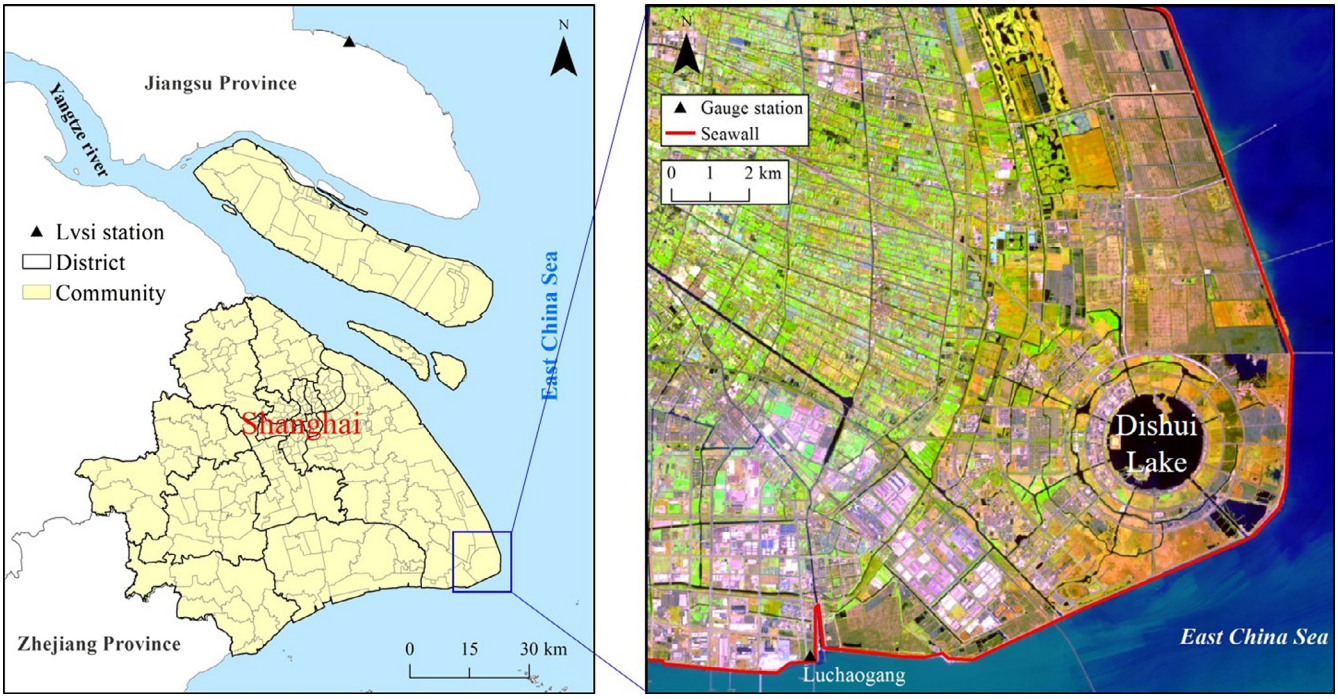

Fig. 1. Location of the study area.

Martinelli, 2002). For example, with a relative SLR from 0.5 m to 1 m predicted by the 2080s, a 100-year flood is projected to occur 2–4 times more often for New York City (Horton et al., 2015).

Advances in InSAR techniques (Massonnet and Feigl, 1998; Higgins, 2016; Mason et al., 2016) and the advent of simplified hydraulic models have enabled high resolution scenario-based flood modeling in the context of SLR and land subsidence. Remotely sensed digital elevation models (DEMs) with varying resolutions have been widely applied for flood modeling (Hinkel et al., 2014; Sampson et al., 2015; Domeneghetti, 2016). Although LiDAR DEMs have optimal resolution and accuracy, they do not have global coverage and are not available over broad areas, particularly in developing countries. Open source DEMs with global coverage, such as Shuttle Radar Topography Mision (SRTM) and Advanced Spaceborne Thermal Emission and Reflection Radiometer Global Digital Elevation Model (ASTER GDEM), have demonstrated remarkable usability for large-scale flood modeling (e.g. Syvitski et al., 2009; Sampson et al., 2015). However, the 90-m SRTM and 30-m ASTER DEMs have significant limitations due to their coarse vertical accuracy (around 12–18 m) (Meyer et al., 2011; Tachikawa et al., 2011; Yang et al., 2011a,b). In recent years, data from the bistatic TanDEM-X satellite mission have enabled the generation of DEMs with a horizontal resolution of 12 m and a vertical accuracy of 2–4 m with global coverage (Krieger et al., 2007). Moreover, time-series Differential Synthetic Aperture Radar Interferometry (DInSAR) have been developed to measure Earth's surface ground displacement over large areas with high spatial resolution, on the order of meters, and with a temporal repetition time of 35 days (ERS and ENVISAT/ASAR sensors) and 6 days (Sentinel-1 sensors) (Berardino et al., 2002; Crosetto et al., 2016). Currently, with a growing number of SAR images collected by different satellite missions with peculiar looking angles and operating wavelengths, long-term (over ten years) three-dimensional displacement time-series can also be retrieved by using multi-satellite DInSAR techniques (Samsonov and d'Oreye, 2012; Pepe et al., 2016a,b). In addition, simplified hydrodynamic models (e.g. LISFLOOD-FP, JFLOW, FloodMap) have been increasingly used for flood modeling at different scales as they can capture the dominant physics of overland flood processes and take input topography in the format of a regular grid. They have been proven to perform as well as full 2-D models for the treatment of coastal flooding (utilizing an unstructured mesh to represent topography), but at a substantially reduced computational cost (Bates et al., 2005; Yin et al., 2016a,b).

In this study, we used the Small Baseline Subset (SBAS) DInSAR technique to jointly analyze SAR data from different sensors together with a simplified hydrodynamic model (FloodMap, Yu and Lane, 2006a,b; Yu and Coulthard, 2015) to investigate the evolving flood risk in a changing climate of Lingang New City in Shanghai, a recently-reclaimed coastal environment. The scenarios used in this paper can be defined as series of events including different flood return periods, sea level and subsidence projections, and future land use in Lingang New City. The main goals of this study are to (i) provide a full characterization of surface changes over time in the coastal delta environment, (ii) derive coastal submerged areas under combined SLR and land subsidence scenarios, and (iii) assess potential coastal flood impacts on a fast growing waterfront urban area. The remainder of this paper is organized as follows. Section 2 describes the study area, whereas Section 3 introduces materials and methods, including the DEM generation, land subsidence measurement, SLR projections, and coastal flood modeling. Section 4 presents the results and discussions. Conclusions and future research directions are provided in Section 5.

2. Study area

Lingang New City, a township at the east end of Shanghai, has been chosen as the study area, because it is highly vulnerable to coastal flooding and has been affected by a significant land subidence over the past decade (Wang et al., 2012). The study site is surrounded by the Yangtze River estuary, East China Sea and Hangzhou Bay (Fig. 1). It covers about 315 km^2 of the southeast part of Pudong New Area with a flat and low-lying topography (on average about 4 m above the Wusong Datum). According to China Sea Level Bulletin (2008,2017), mean sea level in the area has been rising with an average rate of 3.8 mm/a during the past 30 years, and has been empirically estimated as up to 150 mm in the next 30 years. Lingang has been historically experiencing variations in landscape due to changes in natural forcing and intensive human activities, such as sediment deposition, erosion, sand excavation, dam construction and land reclamation (Yang et al.,

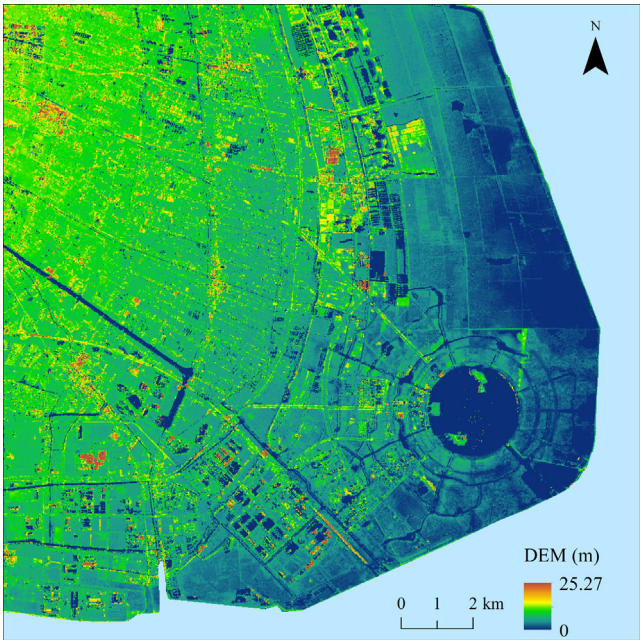

Fig. 2. The generated Tandem-X DEM of the study area.

2011a,b). Human activities have also greatly modified the coastal topography over the past decades. Since 2002, this area has been rapidly developed to be a new sub-center for several functional zones (e.g., a Bonded Logistics Park). A large part of the region (133 km^2), representing approximately 42% of the total area, is sea-reclaimed land (Tian et al., 2016). The subsidence in reclamation areas is dominated by soil compaction mechanisms, which are primarily responsible for vertical movements (Cai et al., 2008; Pepe et al., 2016a; Yu et al., 2017). Natural compaction of loose sediments and self-weight consolidation of dredger fill, under intense urbanization, has caused significant land subsidence in this area.

In history, the area has been frequently affected by cyclonic storms, particularly during the flood season (June to September). For example, during typhoon Winnie (1997), the storm surge peak coincided with an astronomical high tide and resulted in the highest water level in record (5.66 m above Wusong Datum) at Luchaogang gauge station (Fig. 1), and extensive flooding occurred in the coastal floodplain due to levee breach (Liu, 2008). To protect against evolving coastal floods, flood defense system in Lingang were constructed and reinforced several times over the past decades (Fan et al., 2017). In the 1970s, '85′ (i.e., 8 m height and 5 m width levee crest) seawall has been built in response to an extreme coastal flood event that occurred in August 1974. Since the end of the 20th century, higher standard seawall (i.e., around 10 m height) has been constructed to withstand a 200-year storm tide plus wave induced by 12-force winds.

3. Materials and methodology

3.1. DEM generation

The TanDEM-X mission has the innovative capability to simultaneously acquire two SAR satellite images (bistatic acquisition mode) with short along-track baselines, which enables us to derive high-resolution DEMs of the study area. With a pair of TanDEM-X images acquired on 04 November 2012, an up-to-date DEM of our study area, Lingang New City, has been generated using bistatic interferometry. The bistatic acquisition mode is characterized by illumination of an area on the ground by one transmitter and the simultaneous acquisition of the backscattered signals with two receivers. Compared to the monostatic acquisition mode, where only one image is acquired during every overflight of the satellite, temporal decorrelation and atmospheric disturbances, which severely affect the interferometric coherence, are significantly reduced in the TanDEM-X bistatic mode (Gruber et al., 2012). Moreover, since the SAR data pair is simultaneously imaged, the phase contribution due to ground deformation can be neglected. The interferometric phase is simplified in the bistatic interferometry case as follows (Kubanek et al., 2015):

$$\phi = \phi_{ref} + \phi_{topo} + \phi_{noise} \quad (1)$$

where ϕ_{ref} is the phase of the reference surface, i.e., WGS 84 (World Geodetic System 1984) ellipsoid; ϕ_{topo} is the topographic phase; and ϕ_{noise} is the phase noise.

We generated the interferogram with the TanDEM-X pairs using the DORIS software packages (Kampes et al., 2003). The interferometric phase can be expressed as follows (Kubanek et al., 2015):

$$\phi = -\frac{2\pi}{\lambda}\Delta r \quad (2)$$

where Δr is the path length difference between the two (bistatic) SAR acquisitions and λ is the wavelength, which is 3.1 cm for TanDEM-X. Before phase unwrapping, i.e., before resolving the ambiguous phase, a Goldstein filter (Goldstein and Werner, 1998) was applied to smooth the interferometric phase. The filtered interferogram was unwrapped using the SNAPHU (Statistical-Cost Network-Flow Algorithm for Phase Unwrapping) algorithm (Chen and Zebker, 2001). Subsequently, the path length difference of Eq. (2) was converted from phase-to-height (Bamler and Hartl, 1998; Franceschetti and Lanari, 1999):

$$h = -\frac{\lambda}{2\pi}\frac{R\sin\vartheta}{b_\perp}\psi \quad (3)$$

where$b_\perp$ is the orthogonal baseline of the InSAR pair, R is the sensor-to-target slant-range distance, ϑ is the sensor side-looking angle, ψ represents the unwrapped phase relevant to the interferometric phase ϕ (compensated by the phase of the reference plane), and h is the surface height.

The obtained topographic map h is then geocoded to geographic coordinates (WGS 84) using DORIS and gridded using GMT (Wessel et al., 2013). A grid spacing of 6 m is selected for the DEM product and it is further resampled to 18 m resolution to reduce computational costs. Fig. 2 shows the generated Tandem-X DEM of the study area. The theoretical accuracy and actual DEM performance of bistatic TanDEM-X InSAR were verified by Weigt et al. (2012). Their verification shows that for slopes less than 20%, the height error is predicted to be 1.7 m and 2.5 m for a height of ambiguity of 30 m and 45 m, respectively, for the global TanDEM-X data set. Kubanek et al. (2017) obtained a standard deviation of 1.63 m for elevation differences of TanDEM-X DEMs that were generated to study the Tolbachik volcanic complex in Kamchatka, Russia, using the same methodology as used for DEM generation presented in this paper.

3.2. Long-term ground settlement measurement

Advanced time-series DInSAR algorithms can rapidly and regularly detect and measure ground deformation with a high accuracy and at different scales (Ferretti et al., 2001; Berardino et al., 2004; Hooper et al., 2012). DInSAR techniques have, among others, been applied for measuring and mapping ground deformation caused by over-pumping underground water (Gourmelen et al., 2007), tectonic movement (Fattahi et al., 2015), sediments consolidation of river deltas (Aly et al., 2012), and land reclamation (Zhao et al., 2015). Advanced Time-series DInSAR techniques have been proven being effective approaches for accurately measuring ground deformation (Casu et al., 2006; Zhao et al., 2014).

3.2.1. Multi-platform SAR displacement time-series

Three independent sets of SAR images, acquired by different

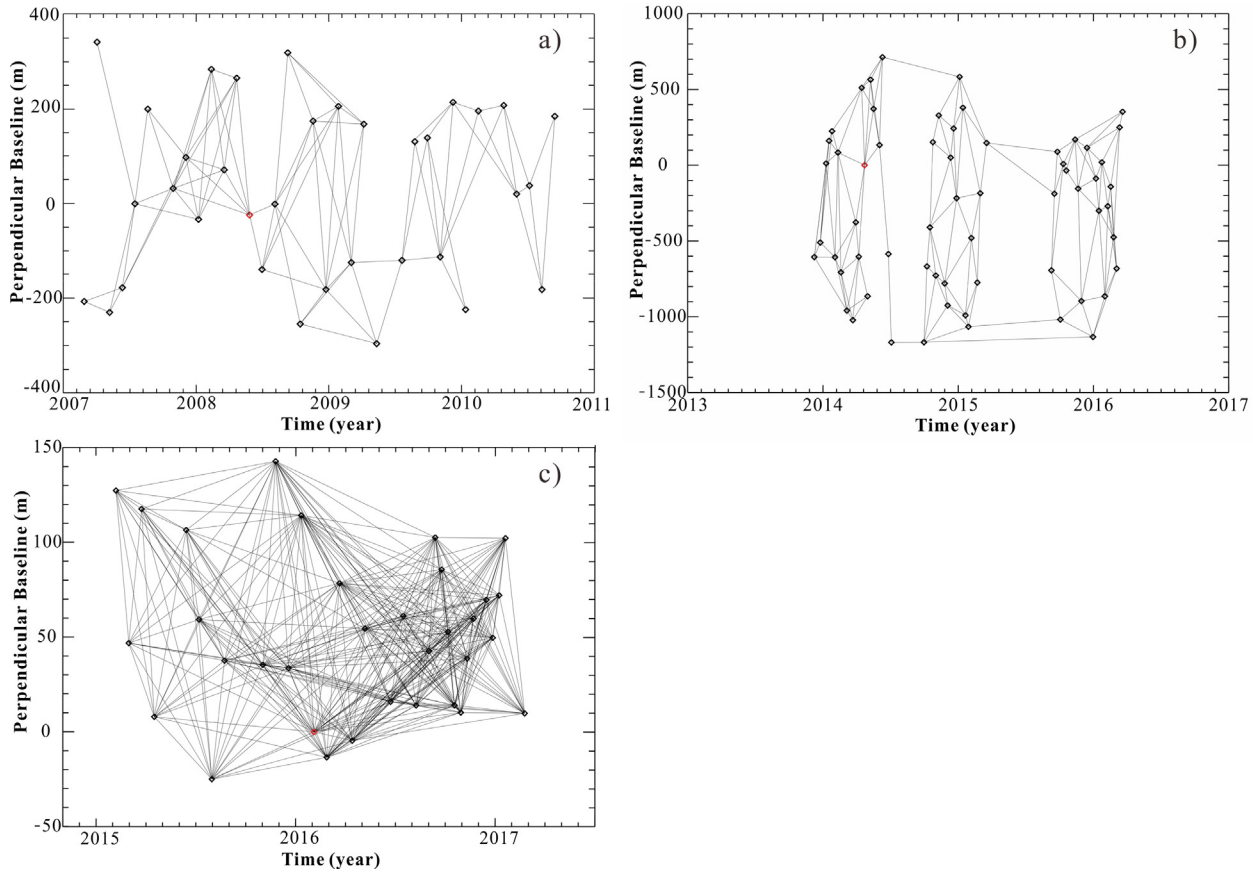

Fig. 3. Distribution of the available ENVISAT ASAR, COSMO-SkyMed, and Sentinel-1A SAR data in the temporal-perpendicular baseline plane, as depicted in (a), (b), and (c) respectively. The master images of ENVISAT ASAR, COSMO-SkyMed, and Sentinel-1A SAR data are represented by red diamonds. (For interpretation of the references to colour in this figure legend, the reader is referred to the web version of this article.)

satellites, were used to retrieve long-term ground displacement of Lingang New City. The former consists of 35 ENVISAT ASAR (ENV) images, acquired with ascending passes from February 26, 2007 to September 13, 2010. The second SAR set is composed of 61 COSMO-SkyMed (CSK) images, which were collected with descending passes from December 7, 2013 to March 18, 2016. The third set was collected by the Sentinel-1A (S1A) satellite with ascending passes from February 26, 2015 to April 4, 2017. All available SAR images were processed through the well-known Small BAseline Subset (SBAS) multi-temporal DInSAR technique, which is outlined in the next subsection.

3.2.2. Small BAseline technique

Small Baseline (SB) techniques are a class of advanced time-series DInSAR methods (Mora et al., 2003; Usai, 2003; Berardino et al., 2002). In particular, the SBAS algorithm (Berardino et al., 2002, Lanari et al., 2007) is one of the well-known and highly used SB techniques. This algorithm is based on selecting a set of small temporal and perpendicular baseline interferograms, thus mitigating decorrelation phenomena, and allows the generation of mean deformation velocity maps and relevant displacement time-series for each coherent point. Fig. 3 (a)-(c) show the distribution of the three groups of SAR images used in this study in the temporal/perpendicular baseline plane. The small baseline interferometric SAR data pairs might be arranged in a few subsets. In order to generate a unique displacement time-series, the phase ambiguities of the differential SAR interferograms are preliminarily resolved, i.e., unwrapped (Costantini and Rosen, 1999, Pepe and Lanari, 2006) and subsequently combined using the singular value decomposition (SVD) method. The residual topographic and atmospheric phase artifacts are also estimated and filtered out. The DInSAR products, i.e., the mean deformation velocity maps and the relevant displacement time-series, are finally geocoded to a common spatial grid. Interested readers can find a detailed description of the SBAS approach and the processing chain in Berardino et al. (2002).

3.2.3. Multi-platform time-series DInSAR

After the SBAS processing of the independent SAR datasets, the unique deformation time-series spanning the acquisition times of the overall SAR datasets is, however, still unknown. Indeed, it should be noted that the deformation time-series are relative to the first SAR acquisition time of each independent dataset. In order to combine the deformation time-series obtained by multi-platforms, we need to determine the multi-platform deformation time-series relative to one global reference time. A methodology has been developed by Pepe et al. (2016a) to combine two time-gapped deformation time-series obtained by ENVISAT ASAR and COSMO-SkyMed SAR datasets. To this aim, the DInSAR-derived line-of-sight (LOS) deformation time-series was first independently projected into vertical deformation time-series by assuming the horizontal (east–west) deformation is negligible. Then, an external geotechnical centrifuge model (Yang et al., 2008), representing a complete time-settlement curve in reclaimed areas of Shanghai, was exploited and fitted to data to jointly estimate the unique deformation time-series over the entire time period between 26 February 2007 and 18 March 2016 (Zhao et al., 2015, Pepe et al., 2016a). Note that deformation due to reclamation can be distinguished in the primary consolidation phase, which takes place immediately after the completion of the reclamation process, and in the secondary compression stage of the alluvial deposit creep of the reclamation fill (Yang et al., 2008), which can last several years after the completion of the reclamation procedures. The used laboratory centrifuge model permits to analyze the temporal evolution of the (vertical) ground displacement due to the

self-weight consolidation (including both the primary and secondary compression stages) of the ocean-reclaimed lands. The used model is expressed as follows (Zhao et al., 2015):

$$s(t) = S_m \frac{(t-\delta)^{\mu}}{k^{\mu} + (t-\delta)^{\mu}} \quad (4)$$

where t represents the consolidation time, S_m is the asymptotic (cumulative) deformation assumed at infinite time (i.e., when the soil consolidation process is ended), δ accounts for the (variable) starting time of the reclamation process, and k and μ are model parameters that influence the shape and curvature of the time-dependent model.

First, the combined ENV + CSK deformation time-series were determined, for each radar pixel, by finding the best-fit between the geotechnical model and the multi-platform deformation time-series. The nonlinear optimization problem was solved efficiently through the (iterative) Levenberg–Marquadt least squares (LS) minimization technique. Subsequently, the Sentinel-1A displacement time-series was independently generated by applying the SBAS technique, converted into (vertical) displacement time-series and finally combined to the previously obtained ENV + CSK displacement time-series. This procedure is repeated for each coherent radar pixel of the investigated scene. Due to the time overlap between the combined ENV + CSK and S1A subsets, the time-series were linked using SVD by extending what was originally proposed in Berardino et al. (2002). Finally, the long-term deformation time-series with a time-span of approximately 10 years (from 2007 to 2018) were obtained. Fig. 4 (a)-(b) show the maps of the asymptotical ground deformation, namely the term of the best-fit model between the combined ENV + CSK and ENV + CSK + S1A displacement time-series and the model, respectively. As evident, there is a good agreement between the two maps, thus indicating that the Levenberg-Marquadt LS optimization procedure is robust to data. Additional remarks and the discussion of the DInSAR results are presented in Section 4.3.

Additionally, some measurements of the displacement affecting the seawalls, as gathered from leveling measurement campaigns in 2009 (Chen et al., 2016), were also available to us. Fig. 5 (a)-(b) shows the vertical mean deformation rate of the seawalls as seen from the leveling and the SBAS measurements (Zhao et al., 2015). It should be noted that we show the distribution of high-coherent pixels seen by ENVISAT in Fig. 5(b) because the available corresponding leveling measurements span approximately the same time period of the ENVISAT acquisitions. The cross comparison between leveling and SBAS data shows a good agreement. Finally, starting from the retrieved parameters and the time vector t of the best-fit model of Equation (3) (see Zhao et al., 2015 for additional information), the expected cumulative deformations (calculated with respect to 26 February 2007) for January 1st of 2030 and 2050, respectively, were predicted.

3.3. Sea level rise projections

Sea level change shows significant local or regional differences due to both climate change and non-climatic factors such as land processes, ocean circulation and atmospheric pressure (Cooper et al., 2008; Hallegatte et al., 2011). Recently, Kopp et al. (2014) presented a global set of probabilistic local sea-level projections which quantified SLR contributions from global processes (e.g., the thermal expansion of ocean water) to local factors (e.g., glacial isostatic adjustment). It has been widely used for flood risk analysis (e.g., Lin and Shullman, 2017). The dataset includes 17 station-based SLR projections in China's coastal areas, among which one station (Lvsi) located at the Yangtze River Estuary. We use the SLR projection of this station in the present study. Compared to the aforementioned statistical SLR studies (e.g. Li et al., 1998), Kopp et al. (2014) show a significant higher rise in local sea level. To account for plausible extreme conditions, we adopted the high-end estimates (i.e., 95th percentiles of model-based distributions) of Kopp's SLR projection at Lvsi for the 2030s (0.31 m) and 2030s (0.61 m), the two future time frames considered in this study.

3.4. Coastal flood modeling

In order to derive coastal flood inundation, FloodMap-Inertial, a well-established 2D hydrodynamic model was employed in this study (Yu and Lane, 2011). This model, as well as an earlier diffusion-based version of it (Yu and Lane, 2006a,b), has been extensively applied in a number of different environments such as coastal regions, urban areas and basins (e.g., Casas et al., 2010; Yin et al., 2013, 2016a,b). It is raster-based and solves the inertial form of the 2D shallow water equations. Flood routing takes the same form as the inertial algorithm of Bates et al. (2010), but with a slightly different method to calculate the time steps. The details of the model are described in Yu and Lane (2011). Therefore, we only focus on the major features of the model.

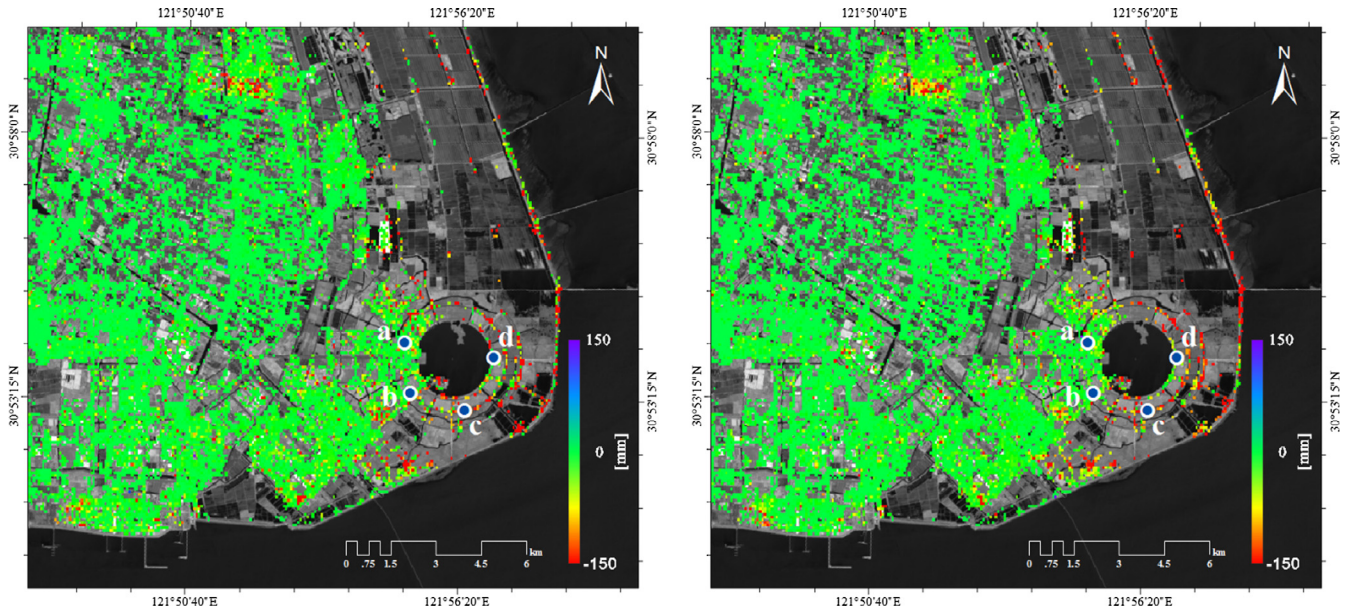

Fig. 4. Maps of asymptotic ground deformation from Nov 2012 to the end time of the consolidation phase derived with the best fit model constrained by ENV + CSK (left) and ENV + CSK + S1A (right).

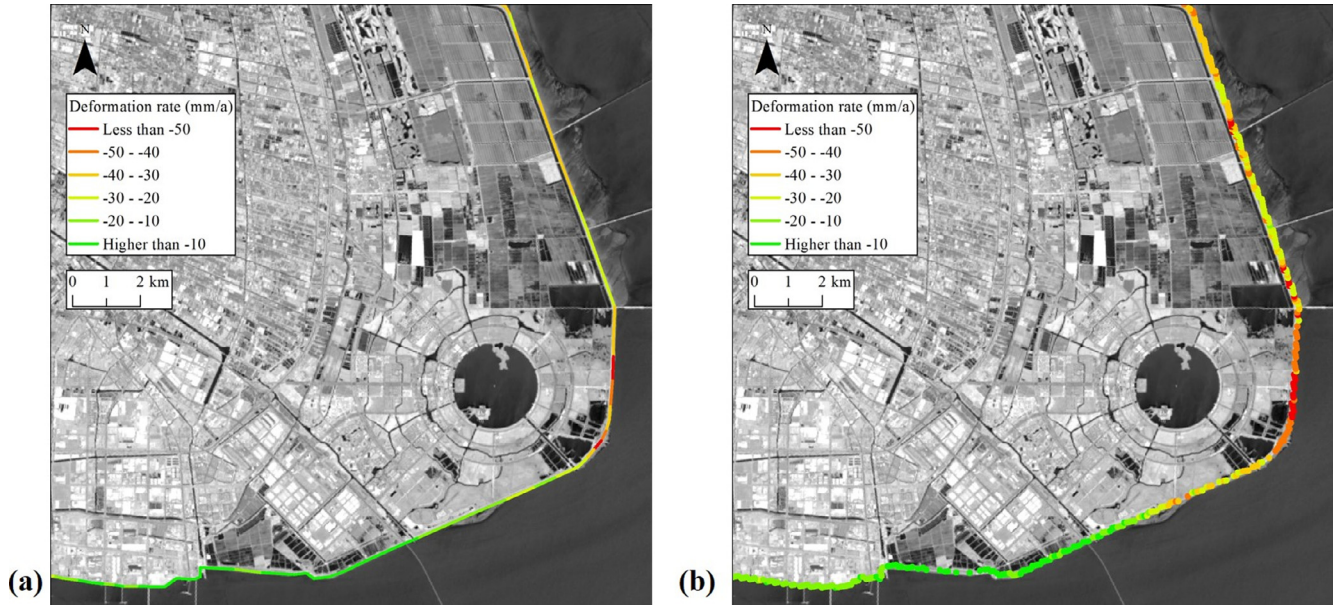

Fig. 5. Vertical deformation rate of the seawall obtained by leveling measurements (a) and SBAS-ENVISAT (b).

Neglecting the convective acceleration term in the Saint-Venant equation, the momentum equation becomes:

$$\frac{\partial q}{\partial t} + \frac{gh\partial(h+z)}{\partial x} + \frac{gn^2q^2}{R^{4/3}h} = 0 \tag{5}$$

where q is the flow per unit width, g is the acceleration due to gravity, R is the hydraulic radius, z is the bed elevation, h is the water depth, and n is the Manning's roughness coefficient. R can be approximated with h for wide and shallow flows. Discretizing the equation with respect to time produces:

$$\frac{q_{t+\Delta t} - q_t}{\Delta t} + \frac{gh_t\partial(h+z)}{\partial x} + \frac{gn^2q_t^2}{h_t^{7/3}} = 0 \tag{6}$$

where one of the q_t in the friction term can be replaced by $q_{t+\triangle t}$, resulting in the explicit expression of the flow at the next time step:

$$q_{t+\Delta t} = \frac{q_t - gh_t\Delta t\left(\frac{\Delta(h_t+z)}{\Delta x}\right)}{(1 + gh_t\Delta tn^2q_t/h_t^{10/3})} \tag{7}$$

The flow in the x and y directions are decoupled and take the same form. Discharge is evaluated at cell edges and depth at the cell center.

To apply FloodMap for coastal flood simulation, time-series of water level along the land-sea boundary are used as input to drive 2D inland flow routing. The shape of the stage hydrograph at the boundary section was derived from the hourly recorded water level available at Luchaogang gauge station during Typhoon Winnie. Assuming tidal cycles remain constant, time-series of the 100- and 1000-year design flood heights above Wusong Datum were generated by scaling Typhoon Winnie's surge heights. To balance the accuracy and computational costs, 24-h stage hydrographs, including two rising phases and two falling limbs, were applied to simulate the coastal flood processes. To account for the effect of SLR, the projected SLRs were linearly added to the state of 2012 to create the flood scenarios for the 2030s and 2030s. Due to lack of available verification materials (e.g., high watermarks and observed flood extent) in the study area, a empirically-based, relatively low floodplain roughness value of 0.03 which corresponds to the n Manning roughness coefficient, was used in the simulations to represent the effect of tidal-flat area and open land on coastal flood routing.

Given the high design standard of seawalls built along the coastline of Shanghai, coastal flooding was not expected to affect the region significantly, assuming seawalls are intact during storm surge events. Comparison of seawall heights (both with and without land deformation) and projected peak surge values suggest that future storm surge events of up to 1000-year magnitude would only affect the region marginally. However, coastal flooding did occur historically (e.g., 1997 Typhon Winnie) along this part of the coastline, due to seawall breaching. Therefore, we generated breaching scenarios based on the actual conditions of the seawalls obtained from a field survey and the observed & projected deformation rates (Figs. 5 and 6). According to 'Code for design of sea dike project (GB/T 51015-2014)' in China, sections with subsidence rates higher than 50 mm/a, which were in particular vulnerable to burst under the combined effect of wave and storm surge, were removed from the seawall system in the simulation.

3.5. Flood sensitivity analysis

Due to the scenario-based nature of this study, we used a theoretically most appropriate roughness value (i.e., 0.03) in flood modeling. However, in the context of flood inundation modeling for historical events, floodplain friction was found to introduce bias into the modeling results. Therefore, model sensitivity to roughness parameterization was evaluated with FloodMap by varying the Manning's n values (between 0.01 and 0.1 at a 0.01 interval).

In order to detect the spatio-temporal changes in flood inundation, two metrics (i.e., Fit statistic (F) and Root Mean Square Deviation (RMSD)) were used to quantify the degree of matching and variation between model predictions respectively. In each case, the n = 0.01 simulation was used as the reference and both measures are calculated against this reference. F is widely used for evaluating the goodness of agreement between predicted flood extent and the reference (Bates and De Roo, 2000; Horritt and Bates, 2001; Yu and Lane, 2006a,b). It varies between 1 for a perfect fit and 0 when no overlap exists. It can be calculated as follows:

$$\mathrm{F} = \frac{A_o}{A_r + A_s - A_o} \tag{8}$$

where A_r is the referenced wet areas, A_s is the predicted wet areas, and A_o is the overlap of A_r and A_s.

The RMSD is particularly suitable for evaluating the overall agreement/discrepancy of water depth between two paired results on a cell-by-cell basis (Yu and Lane, 2011; Yin et al., 2016a,b). It can be defined

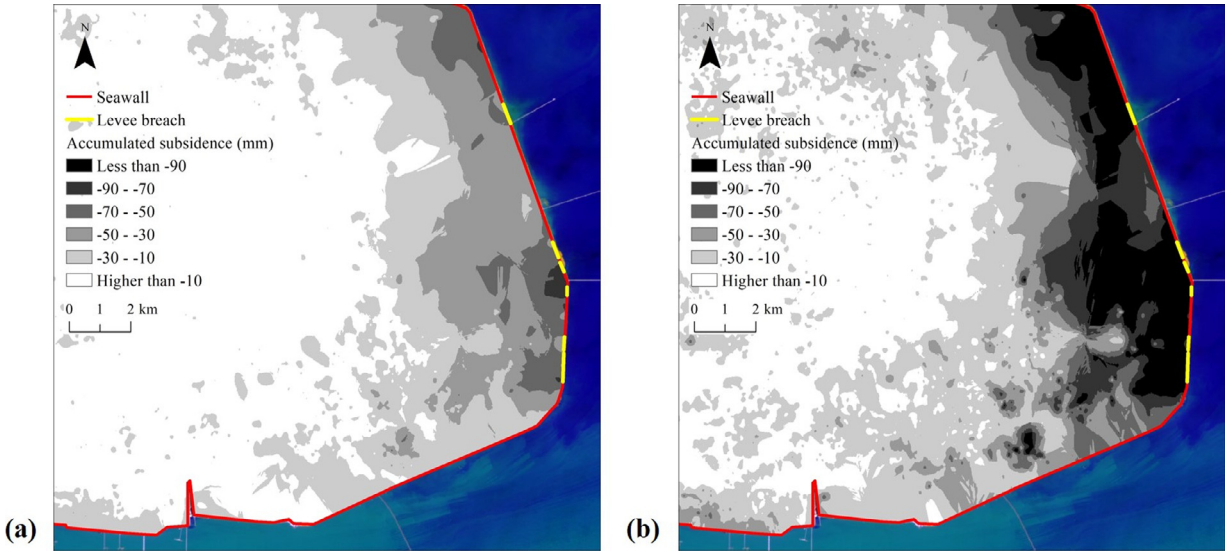

Fig. 6. Accumulated ground deformation projections for 2030s (a) and 2050s (b) in Lingang New City.

as follows:

$$\text{RMS D}= \sqrt{\frac{\sum_{i=0}^{n} (d_i^s - d_i^r)^2}{n}} \quad (9)$$

where d_i^s and d_i^r are the predicted and referenced water levels (or depths) respectively, i is the index of the wet cells and n is the total number of wet cells in the prediction and observation.

4. Results and discussions

4.1. Coastal inundation mapping

Predicted maximum inundation depths for 100-year and 1000-year coastal flood scenarios due to hypothetical levee breaches for the present (i.e., 2012), the 2030s and the 2030s are shown in Fig. 7 and the maximum flooded areas are summarized in Table 1. The mean maximum flood depth in the table represents the average value of maximum flood depths in all grids during the flood model run. Comparison of the derived inundation maps leads to two important findings. First, similar inundation pattern are generally observed for both simulations (one in 100- and 1000-year return periods) in the study area, but with different flood depths. This can be largely attributed to the topographic confinement of the coastal floodplain. The levee-breach flow would be blocked by the previous seawall (Fan et al., 2017), and thus the water would be mostly confined within the coastal flat and low-lying areas where land was only recently reclaimed in the past decade (Zou et al., 2007). In addition, Dishui Lake which has a total area of 5.56 km^2 and a storage of 16.2 million m^3, also shows a significant impact on the detention and storage of the storm water, restricting further inland propagation of coastal flood waves.

Second, our results show that rapid sea-level rise combined with extensive land subsidence generally leads to minor but non-linear impacts on coastal inundation over time in our study area. For example, when the 0.44 m and 0.89 m rise in the relative sea level (i.e. the sum of SLR and subsidence projections) for the 2030s and the 2030s are considered, a 6% and 15% increase in predicted maximum inundation area can be observed for future 100-year flood events. Similarly, compared to 2012, the mean water depths are projected to rise 0.11 m (8%) by 2030 and 0.23 m (17%) by 2050, respectively. In contrast, the impact of the projected relative sea level rise appears to be more pronounced for 1000-year flood events, where the total flood area is expected to increase by 23% by 2050; the maximum water depth will rise by 21%. Although mean land subsidence only makes up around 30% of the relative sea level rise, coastal flooding response is also controlled by a non-uniform pattern of subsidence. It was found that rapid subsidence would further accentuate inundation extent and depth in the reclamation area, making it more vulnerable to coastal flooding.

In order to detect the temporal changes of coastal flood dynamics, the time evolution of predicted inundation areas for all scenarios are presented in Fig. 8. The curves mostly coincide during the initial wetting phase (up to 7 h), suggesting that levee-breach water flow extends progressively overland before and after the first flood peak, due to the mild relief and flat topography of the coastal floodplain. After the rapid inland intrusion in each simulation, the inundated area increases only slightly with a much higher stage during the second rising phase, indicating that further widespread expansion of coastal flooding is limited due to strong resistance from surface obstruction. This finding also confirms the topographic confinement of the coastal floodplain, which we identified in Fig. 2. Moreover, as shown in Fig. 8, the general pattern of simulated time series revealed that the temporal characteristics of the inundated area is not strictly synchronous with the timing of the tidal cycle. In most cases, the flood extent continues to increase even as the stage recedes, because the floodwater level greatly overwhelmed low-lying waterfront ground. Another important finding is that the relative SLR provides an elevated base for a storm flood to build upon and SLR and land subsidence may lead to more pronounced impact on coastal inundation during the falling limbs of tidal hydrograph (Yin et al., 2013).

4.2. Coastal flood impacts

Coastal floodings, as derived by our models, will affect areas of current and future land use, where data are officially provided by the Shanghai Institute of Surveying and Mapping (Fig. 9). An immediate finding is that although the Lingang area has experienced rapid urbanization during the last decade, wetlands and bare lands mainly dominate the floodplain and therefore flood impacts have a minor effect on the coastal communities. At present, considerable personal injury and property damage are unlikely to occur in this area. However, according to the land use planning for Lingang New City, the process of urbanization and floodplain development is expected to accelerate in the near future. According to the Lingang New City Plan, the total population is expected to rise from about 50–100 thousand today to 1–1.5 million in the next decades. Thus rapid expansion in human settlements is expected to occupy the waterfront areas around Dishui Lake. If long term subsidence combined with strong storm tide causes the emergence of

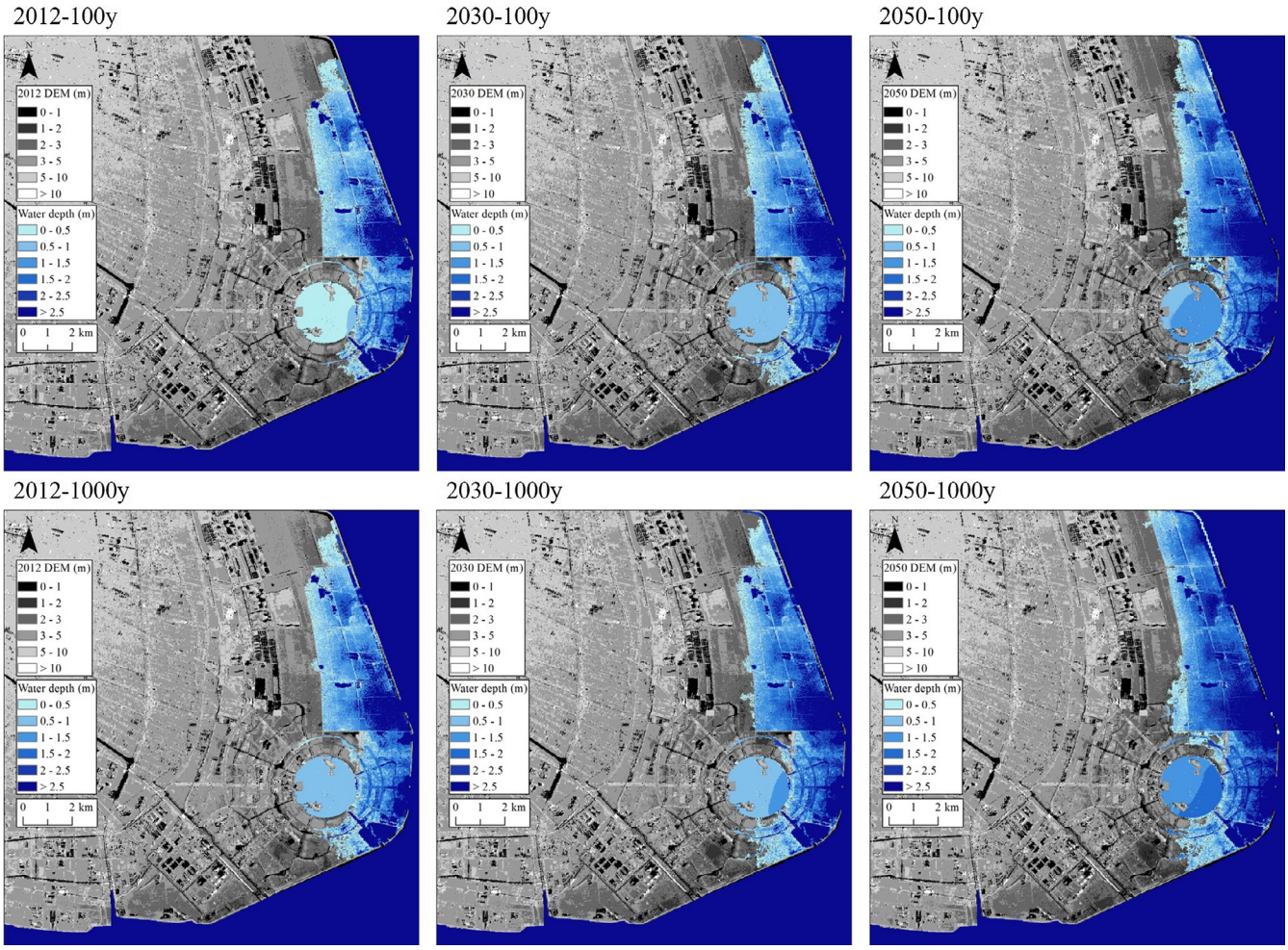

Fig. 7. Potential levee-breach 100-year and 1000-year coastal flood inundation scenarios modeled with up-to-date and high resolution DEM and long-term DInSAR derived ground deformation time series for Lingang New City of Shanghai in 2012, the 2030s and the 2050s.

levee breach, extensive coastal flood inundation would occur throughout the area in the 2030s and 2030s, leading to significant casualties and losses. In addition, future flood risk could also be significant in the northern part of the coastal floodplain, where comprehensive industrial, research & development, service, and residential areas may be constructed in the future. Compared to the direct impacts, possible indirect consequences, such as interruption of public services or negative influences on industrial production and living, would be more pronounced. The indirect impacts may last a few days to even a few months after an extreme event (Yin et al., 2016b).

4.3. Uncertainty and limitations

Uncertainties are inherent in a changing environment. In our study, the long term flood-risk mappings could be highly uncertain due to the assumptions and limitations associated with data and methods used here. First, in terms of SLR projections, the response of the Greenland and the West Antarctic ice sheets to future global warming is the largest long-term source of uncertainty. Although the likelihood of the ice sheet collapse within the coming century has been described as extremely low (black swan, i.e., an event or occurrence that deviates beyond what is normally expected of a situation and is extremely difficult to predict), a partial or complete collapse of the Western Antarctic Ice Sheet will cause the global mean sea level to rise up to 4 m (Bentley, 1998; Vaughan and Spouge, 2002; Pfeffer et al., 2008; Bamber et al., 2009; Ritz et al., 2015). Second, coastal storminess is projected to change with climate change (Lin et al., 2012, 2015). Future frequency of extreme storms is very likely to increase until 2100 (IPCC, 2012). It is yet unclear how a changing storminess, in combination with SLR, will affect the frequency and intensity of coastal flooding in Shanghai. Third, the flood modeling conducted in this study is based upon an arbitrary assumption that levee breaches will occur in the locations/

Table 1
The areas (km^2 and percentage of computation domain) and depths subject to different levee-breach coastal flood scenarios under sea level rise and land subsidence projections for Lingang New City, Shanghai.

Time	High-end sea level rise (m)	Mean land subsidence (m)	Maximum flood areas (km^2) and percentage (%)		Mean maximum flood depths (m)	
			100y flood	1000y flood	100y flood	1000y flood
2012	/	/	32.79 (13.14%)	34.30 (13.74%)	1.33	1.45
2030	0.31	0.13	34.72 (13.91%)	36.37 (14.57%)	1.44	1.59
2050	0.61	0.28	37.76 (15.13%)	42.18 (16.90%)	1.56	1.76

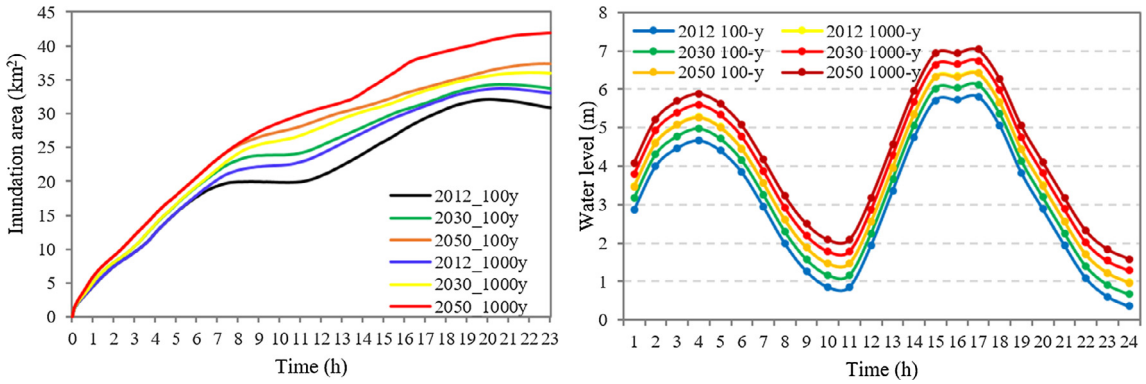

Fig. 8. Time series of inundation extents and water levels with 100-year and 1000-year flood return periods in 2012, 2030s and 2030s for Lingang New City of Shanghai.

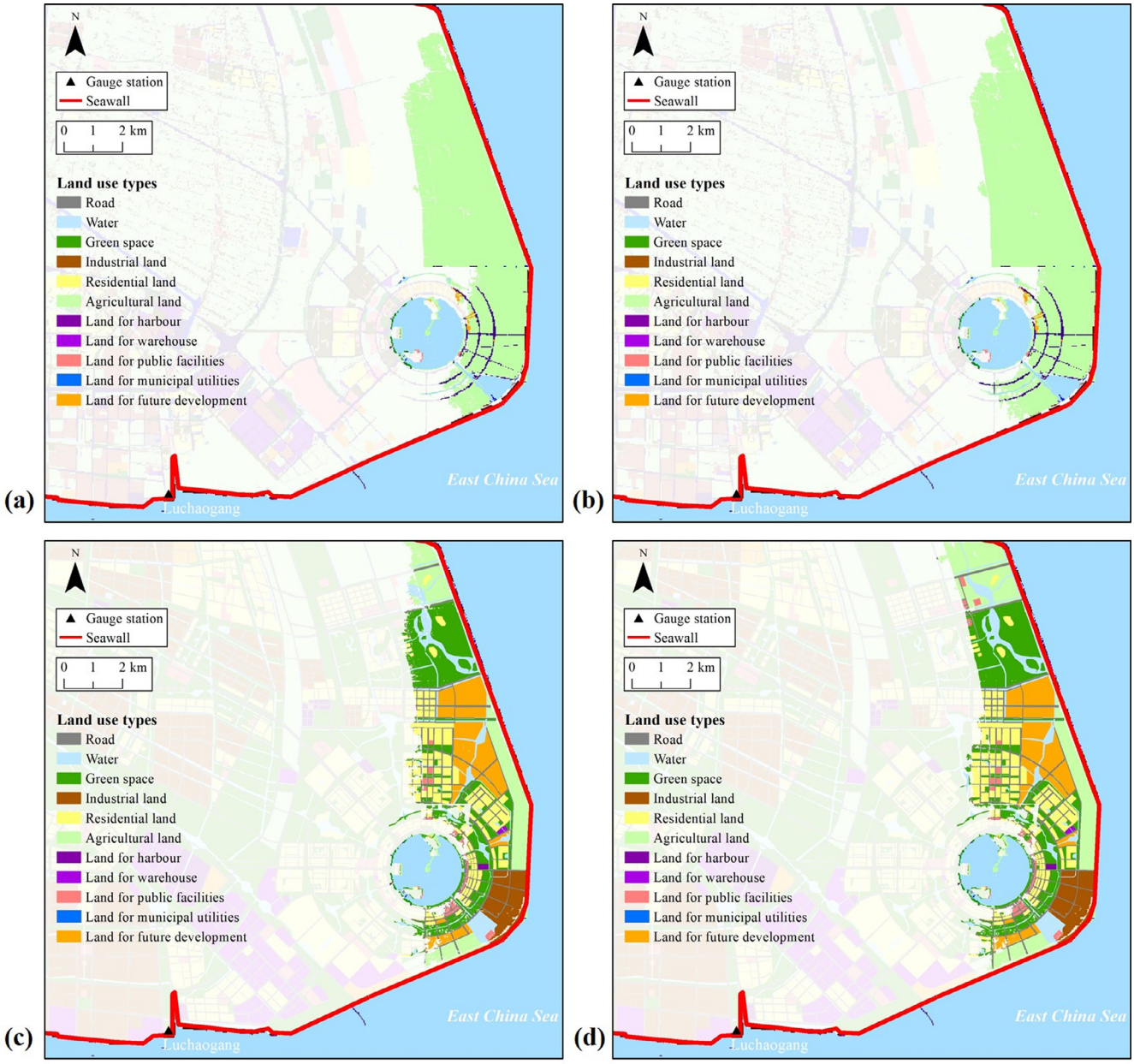

Fig. 9. Land uses/planning fall within the predicted inundation areas (highlight) at current and future states: (a) 100y flood in 2012; (b) 1000y flood in 2012; (c) 100y flood in 2030s; and (d) 1000y flood in 2030s.

sections with an observed subsidence rate higher than 50 mm/a. There are certain limitations and errors associated with such hypothesis, as the mechanism of seawall failure is determined by different triggering factors, including material and structure of the seawall, geologic conditions, and hydrodynamics (e.g., waves). The impacts of land subsidence on the stability of seawall and the threshold of levee breaches should be explicitly tested and verified.

Another source of uncertainty arises from the long-term (over twenty years) ground deformation projections. Although the long-term vertical deformation is predicted with best-fit models, which are obtained using the time-dependency laboratory models constrained by multi-platform DInSAR measurements (Pepe et al., 2016b), uncertainties in estimating the asymptotic values of deformation might depend on the temporal length of the available, constrained DInSAR time-series. The longer the DInSAR displacement time-series the more accurate is the fit between the DInSAR data and the foreseen models. To get an idea of such uncertainties, we calculated the asymptotic ground deformation values of each high coherent point from November 2012 until the end of the consolidation phases with the best-fit models constrained by the combined ENV + CSK and ENV + CSK + S1A deformation time-series. As anticipated in Section 3.2.3, Fig. 4 shows the maps of asymptotic ground deformation, indicating that the asymptotic values of deformation agree well with the best fit models derived by ENV + CSK and ENV + CSK + S1A in most of the study areas. Most of the points with different asymptotic values (see Equation (3)) of deformation are located along the seawall and the east of Dishui Lake. In particular, Table 2 presents the asymptotic values of deformation at four points labeled as a, b, c, d in Fig. 4. According to the quantity values of uncertainties in ground deformation prediction, the observed deviation is acceptable for the long-term flood-risk mapping. It is worth remarking that our predictions are based on the analysis of only ten years of data, and are relevant to a very dynamical coastal area that is highly affected by human activities. More lands are expected to be reclaimed along the current coastline in future decades. Accordingly, continuous DInSAR measurements are necessary for monitoring and progressively measuring the changes and for updating the projections.

Flood model uncertainties have been addressed and time-series of F-statistic and RMSD for each simulation are shown in Fig. 10. The results show significant variations in the spatio-temporal pattern between individual simulations and the n = 0.01 reference, suggesting the model's strong sensitivity to floodplain roughness. Another finding is that with higher Manning's n values, the differences in inundation area and depth becomes less pronounced throughout the simulations, especially in terms of RMSD. The sensitivity of the RMSD is progressively magnified as the flood magnitude increases over time. On the contrary, higher magnitude flood events (e.g., 1000-year floods) appear to be less sensitive to roughness due to the lateral confinement of the floodplain. This observation reveals that coastal flood inundation is highly uncertain in the rapidly developing area, particularly for long-term predictions.

5. Conclusions

This paper demonstrates a novel approach to evaluate evolving flood hazard in the context of sea level rise and land subsidence for Lingang New City in Shanghai through an integration of 2D numerical flood modeling and InSAR techniques. A number of conclusions can be drawn from the results obtained in this study. First, even with rapid sea level rise and extensive land subsidence in the future, coastal flood inundation due to potential levee breach is predicted to occur mostly in the waterfront low-lying areas, because of topographic confinement in the floodplain and blockage of previous seawalls. Second, flood impacts in this area are expected to be minor due to a very low exposure of the population and property at present, but future flood risk could be significantly higher as rapid urbanization and large-scale coastal development have been planned in the floodplain. Finally, limitations, biases and even errors in local SLR projections, storm climatology projections, levee breach estimations, ground deformation predictions, and coastal flood modeling may have induced substantial uncertainties in the final estimates.

The methodology proposed here could be applied to other coastal communities facing significant SLR, subsidence and flooding challenges. It may contribute to a better understanding of the long-term coastal flood hazard at local scale, and thus help to develop sustainable flood risk management in coastal communities. However, to derive more robust conclusions, further research should include: (1) analyzing the mechanisms and probabilities of seawall failure to provide a more complete picture of levee breach; (2) evaluating the impacts of extreme SLR scenarios (e.g., collapse of the West Antarctic Ice Sheet) and projected storminess due to climate change on coastal flooding; (3) coupling soil compaction mechanics with time-series InSAR measurements to generate more reliable long-term ground deformation predictions; (4) incorporating the 'crowd sourced' data and/or Unmanned Aerial Vehicle (UAV) remote sensing maps into flood model calibration and validation, and (5) conducting quantitative assessment of coastal flood risk as well as cost-benefit analysis of adaptation measures to support decision making with respect to financial investment. Finally, great efforts are required to improve the accuracies in the datasets, models and future scenarios applied to coastal flood risk analysis.

Acknowledgments

This work was supported by the National Key Research and Development Program of China (Grant no: 2017YFE0100700), the National Natural Science Foundation of China (Grant no: 41871164; 41801337; 51761135024), the Humanities and Social Science Project of Education Ministry of China (Grant no: 17YJAZH111), the Research Grants of Science and Technology Commission of Shanghai Municipality through Project 18ZR1410800, the UK Natural Environment Research Council under the Environmental Risks to Infrastructure Innovation Program (Grant no: NE/M008770/1; NE/N013050/1; NE/R009600/1), the Key Laboratory of Land Subsidence

Table 2
Total cumulative deformation values and end time values of consolidation phases between the best-fit models retrieved by using the combined ENV-CSK time series and the ones extracted from the combined ENV-CSK-S1A time series. The end of consolidation phase has been considered, for each radar pixel, as the time in correspondence to which the expected surface displacement rate is smaller than 0.5 mm/year.

		Best fit model derived with ENV + CSK	Best fit model derived with ENV + CSK + S1A
a	End time of consolidation	2015	2015
	Asymptotic values of ground subsidence (mm)	2	2
b	End time of consolidation	2030	2031
	Asymptotic values of ground subsidence (mm)	62	60
c	End time of consolidation	2035	2035
	Asymptotic values of ground subsidence (mm)	93	109
d	End time of consolidation	2060	2057
	Asymptotic values of ground subsidence (mm)	118	109

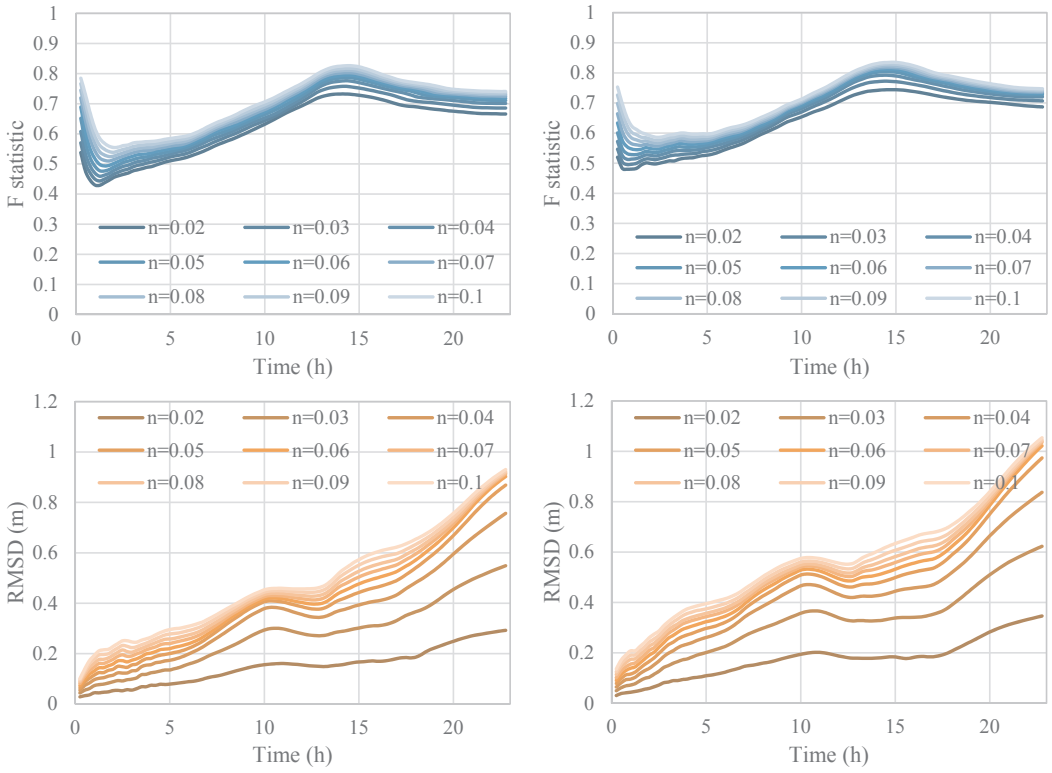

Fig. 10. Time series of F statistic, and depth RMSD for current 100- (left column) and 1000-year (right column) flood simulations with different Manning's n values.

Monitoring and Prevention, Ministry of Land and Resources through Project KLLSMP201503, the Fund of the Director of the Key Laboratory of Geographic Information Science (Ministry of Education), East China Normal University (Grant no: KLGIS2017C03), and the National Science Foundation of the United States (EAR-1520683). This work has been performed within the Dragon 4 ESA project ID 32294. Cosmo-SkyMed SAR data were provided to us by the Italian Space Agency in the framework of the Dragon III project ID 10644 and TanDEM-X data were provided by the German Aerospace Center (DLR) under proposal NTI_INSA0405. Sentinel-1A data were freely downloaded from the ESA Sentinel Hub.

References

Aly, M.H., Klein, A.G., Zebker, H., 2012. Land Subsidence in the Nile Delta of Egypt by persistent scatterer interferometry. Remote Sens. Lett. 3 (7), 621–630.
Antonioli, F., Anzidei, M., Amorosi, A., Presti, V.L., Mastronuzzi, G., Deiana, G., 2017. Sea-level rise and potential drowning of the Italian coastal plains: flooding risk scenarios for 2100. Quat. Sci. Rev. 158, 29–43.
Bamber, J.L., Riva, R.E., Vermeersen, B.L., Lebrocq, A.M., 2009. Reassessment of the potential sea-level rise from a collapse of the west Antarctic ice sheet. Science 324 (5929), 901–903.
Bates, P.D., Roo, A.P.J.D., 2000. A simple raster-based model for flood inundation simulation. J. Hydrol. 236 (1), 54–77.
Bates, P.D., Dawson, R.J., Hall, J.W., Horritt, M.S., Nicholls, R.J., Wicks, J., Hassan, M.A.A.M., 2005. Simplified two-dimensional numerical modeling of coastal flooding and example applications. Coast. Eng. 52, 793–810.
Bates, P.D., Horritt, M., Fewtrell, T., 2010. A simple inertial formulation of the shallow water equations for efficient two-dimensional flood inundation modeling. J. Hydrol. 387 (1), 33–45.
Bamler, R., Hartl, P., 1998. Synthetic aperture radar interferometry. Inverse Prob. 14, R1–R54.
Berardino, P., Fornaro, G., Lanari, R., Sansosti, E., 2002. A new algorithm for surface deformation monitoring based on small baseline differential SAR interferograms. Geosci. Remote Sens. IEEE Trans. 40 (11), 2375–2383.
Bentley, C.R., 1998. Rapid sea-level rise from a west Antarctic ice-sheet collapse: a short-term perspective. J. Glaciol. 44 (146), 157–163.
Cai, J., Wang, J., Wu, J., Hu, C., Grafaren, E., Chen, J., 2008. Horizontal deformation rate analysis based on multiepoch GPS measurements in Shanghai. J. Surv. Eng. 134, 132–137.
Casu, F., Manzo, M., Lanari, R., 2006. A quantitative assessment of the SBAS algorithm performance for surface deformation retrieval from DInSAR data. Remote Sens. Environ. 102 (3), 195–210.
Carminati, E., Martinelli, G., 2002. Subsidence rates in the Po Plain, northern Italy: the relative impact of natural and anthropogenic causation. Eng. Geol. 66 (3), 241–255.
Casas, A., Lane, S.N., Yu, D., Benito, G., 2010. A method for parameterising roughness and topographic sub-grid effects in hydraulic modeling from LiDAR data. Hydrol. Earth Syst. Sci. 14 (8), 1567–1579.
Cayan, D.R., Bromirski, P.D., Hayhoe, K., Tyree, M., Dettinger, M.D., Flick, R.E., 2008. Climate change projections of sea level extremes along the california coast. Clim. Change 87 (1), 57–73.
Chen, C.W., Zebker, H.A., 2001. Two-dimensional phase unwrapping with use of statistical models for cost functions in nonlinear optimization. J. Opt. Soc. Am. A 18 (2), 338–351.
Chen, Y., Shi, Y., Li, B., Yu, J., 2016. Seawall subsidence in Shanghai: characteristics and driving mechanisms. Marine Geol. Quatern. Geol. 6, 71–78 (in Chinese).
Cooper, M.J., Beevers, M.D., Oppenheimer, M., 2008. The potential impacts of sea level rise on the coastal region of New Jersey, USA. Clim. Change 90, 475–492.
Costantini, M., Rosen, P. A., 1999. A generalized phase unwrapping approach for sparse data. In: Geoscience and Remote Sensing Symposium, 1999. IGARSS '99 Proceedings. IEEE 1999 International, Hamburg, pp. 267–269.
Crosetto, M., Monserrat, O., Cuevas-González, M., Devanthéry, N., Crippa, B., 2016. Persistent Scatterer Interferometry: a review. ISPRS J. Photogramm. Remote Sens. 115, 78–89.
Domeneghetti, A., 2016. On the use of SRTM and altimetry data for flood modeling in data-sparse regions. Water Resour. Res. 52 (4), 2901–2918.
Ericson, J.P., Vörösmarty, C.J., Dingman, S.L., Ward, L.G., Meybeck, M., 2006. Effective sea-level rise and deltas: causes of change and human dimension implications. Global Planet. Change 50, 63–82.
Fan, D., Wu, Y., Zhang, Y., Burr, G., Huo, M., Li, J., 2017. South flank of the Yangtze Delta: past, present, and future. Mar. Geol. 392, 78–93.
Fattahi, H., Amelung, F., Chaussard, E., Wdowinski, S., 2015. Coseismic and postseismic deformation due to the 2007 M5.5 Ghazaband fault earthquake, Balochistan, Pakistan. Geophys. Res. Lett. 42, 3305–3312.
Ferretti, C., Prati, C., Rocca, F., 2001. Permanent scatterers in SAR interferometry. IEEE Trans. Geosci. Remote Sens. 39 (1), 8–20.
Franceschetti, G., Lanari, R., 1999. Synthetic Aperture Radar Processing. CRC Press.
Goldstein, R.M., Werner, C.L., 1998. Radar interferogram filtering for geophysical applications. Geophys. Res. Lett. 25 (21), 4035–4038.
Gourmelen, N., Amelung, F., Casu, F., Manzo, M., Lanari, R., 2007. Mining-related ground deformation in Crescent Valley, Nevada: implications for sparse GPS networks. Geophys. Res. Lett. 34 (9), 252–254.
Grilli, A., Spaulding, M.L., Oakley, B.A., Damon, C., 2017. Mapping the coastal risk for the next century, including sea level rise and changes in the coastline: application to Charlestown RI, USA. Natl. Hazards 4, 1–26.
Gruber, A., Wessel, B., Huber, M., Roth, A., 2012. Operational TanDEM-X DEM calibration and first validation results. ISPRS J. Photogramm. Remote Sens. 73 (6), 39–49.
Hallegatte, S., Ranger, N., Mestre, O., Dumas, P., Corfee-Morlot, J., Herweijer, C., Wood,

R., 2011. Assessing climate change impacts, sea level rise and storm surge risk in port cities: a case study on Copenhagen. Clim. Change 104 (1), 113–137.
Hay, C.C., Morrow, E., Kopp, R.E., Mitrovica, J.X., 2015. Probabilistic reanalysis of twentieth-century sea-level rise. Nature 517, 481–484.
Hinkel, J., Lincke, D., Vafeidis, A.T., Perrette, M., Nicholls, R.J., Tol, R.S.J., 2014. Coastal flood damage and adaptation costs under 21st century sea-level rise. PNAS 111 (9), 3292–3297.
Higgins, S.A., 2016. Review: Advances in delta-subsidence research using satellite methods. Hydrogeol. J. 24 (3), 587–600.
Hooper, A., Bekaert, D., Spaans, K., Arıkan, M., 2012. Recent advances in SAR interferometry time series analysis for measuring crustal deformation. Tectonophysics 514, 1–13.
Horritt, M.S., Bates, P.D., 2001. Effects of spatial resolution on a raster based model of flood flow. J. Hydrol. 253 (1–4), 239–249.
Horton, R., Little, C., Gornitz, V., Bader, D., Oppenheimer, M., 2015. New York City Panel on Climate Change 2015 Report Chapter 2: Sea Level Rise and Coastal Storms. Annals of the New York Academy of Sciences, vol. 1336, pp. 36–44.
IPCC, 2012. In: Field, C.B., Barros, V., Stocker, T.F., Qin, D., Dokken, D.J., Ebi, K.L., Mastrandrea, M.D., Mach, K.J., Plattner, G.K., Allen, S.K., Tignor, M., Midgley, P.M. (Eds.), A Special Report of Working Groups I and II of the Intergovernmental Panel on Climate Change. Cambridge University Press, Cambridge, pp. 582.
IPCC, 2014. Climate Change 2014: Synthesis Report. Contribution of Working Groups I, II and III to the Fifth Assessment Report of the Intergovernmental Panel on Climate Change [Core Writing Team, R.K. Pachauri and L.A. Meyer (eds)]. IPCC, Geneva, Switzerland, pp. 151.
Jelgersma, S., 1996. Land subsidence in coastal lowlands. In: Milliman, J.D., Haq, B.U. (Eds.), Sea Level Rise and Coastal Subsidence. Kluwer Acad., Dordrecht, Netherlands, pp. 47–62.
Karegar, M.A., Dixon, T.H., Malservisi, R., Kusche, J., Engelhart, S.E., 2017. Nuisance flooding and relative sea-level rise: the importance of present-day land motion. Sci. Rep. 7 (1), 11197.
Kopp, R.E., Horton, R.M., Little, C.M., 2014. Probabilistic 21st and 22nd century sea-level projections at a global network of tide-gauge sites. Earths Future 2 (8), 383–406.
Krieger, G., Moreira, A., Fiedler, H., Hajnsek, I., Werner, M., Younis, M., 2007. TanDEM-X: a satellite formation for high-resolution SAR interferometry. IEEE Trans. Geosci. Remote Sens. 45, 3317–3341.
Kubanek, J., Westerhaus, M., Schenk, A., Aisyah, N., Brotopuspito, K.S., Heck, B., 2015. Volumetric change quantification of the 2010 merapi eruption using TanDEM-X InSAR. Remote Sens. Environ. 164, 16–25.
Kubanek, J., Westerhaus, M., Heck, B., 2017. TanDEM-X time series analysis reveals lava flow volume and effusion rates of the 2012–2013 Tolbachik, Kamchatka fissure eruption. J. Geophys. Res. Solid Earth 122, 7754–7774.
Lanari, R., Casu, F., Manzo, M., Zeni, G., Berardino, P., Manunta, M., 2007. An overview of the small baseline subset algorithm: a DInSAR technique for surface deformation analysis. Pure Appl. Geophys. 164 (4), 637–661.
Li, Y., Qin, Z., Duan, Y., 1998. An estimation and assessment of future sea level rise in Shanghai region. Acta Geographica Sinica 53, 393–403 (in Chinese).
Lin, N., Emanuel, K., Oppenheimer, M., Vanmarcke, E., 2012. Physically based assessment of hurricane surge threat under climate change. Nat. Clim. Change 2 (6), 462–467.
Lin, N., Shullman, E., 2017. Dealing with hurricane surge flooding in a changing environment: part I. Risk assessment considering storm climatology change, sea level rise, and coastal development. Stoch. Env. Res. Risk Assess. 31 (9), 2379–2400.
Little, C.M., Horton, R.M., Kopp, R.E., Oppenheimer, M., Vecchi, G.A., Villarini, G., 2016. Joint projections of US East Coast sea level and storm surge. Nat. Clim. Change 5 (12), 1114–1120.
Liu, X., 2008. Shanghai flood prevention handbook. Shanghai Popular Science Press, Shanghai (in Chinese).
Mason, D.C., Trigg, M., Garcia-Pintado, J., Cloke, H.L., Neal, J., Bates, P.D., 2016. Improving the TanDEM-X Digital Elevation Model for flood modeling using flood extents from Synthetic Aperture Radar images. Remote Sens. Environ. 173, 15–28.
Massonnet, D., Feigl, K.L., 1998. Rader interferometry and its application to changes in the Earth's surface. Rev. Geophys. 36, 441–500.
Meyer, D.J., Tachikawa, T., Abrams, M., Tsu, H., Hato, M., Gesch, D.B., 2011. The ASTER Global Digital Elevation Model version 2.0 – Early Validation Results. AGU Fall Meeting, vol. 20. AGU Fall Meeting Abstracts , pp.1442.
Mills, M., Mutafoglu, K., Adams, V.M., Archibald, C., Bell, J., Leon, J.X., 2016. Perceived and projected flood risk and adaptation in coastal southeast Queensland, Australia. Climatic Change 136 (3–4), 523–537.
Mora, O., Mallorqui, J.J., Broquetas, A., 2003. Linear and nonlinear terrain deformation maps from a reduced set of interferometric SAR images. IEEE Trans. Geosci. Remote Sens. 41 (10), 2243–2253.
Orton, P., Vinogradov, S., Georgas, N., Blumberg, A., Lin, N., Gornitz, V., Little, C., Jacob, K., Horton, R., 2015. New York City Panel on Climate Change 2015 Report Chapter 4: Dynamic coastal flood modeling. Annals of the New York Academy of Sciences, vol. 1336, no. 1, pp. 56–66.
Oppenheimer, M., Alley, R.B., 2016. How high will the seas rise? Science 354, 1375–1377.
Paprotny, D., Terefenko, P., 2017. New estimates of potential impacts of sea level rise and coastal floods in Poland. Nat. Hazards 85, 1259–1277.
Pepe, A., Lanari, R., 2006. On the extension of the minimum cost flow algorithm for phase unwrapping of multitemporal differential SAR interferograms. IEEE Trans. Geosci. Remote Sens. 44 (9), 2374–2383.
Pepe, A., Solaro, G., Calo, F., Dema, C., 2016a. A minimum acceleration approach for the retrieval of multiplatform InSAR deformation time series. IEEE J. Sel. Top. Appl. Earth Obs. Remote Sens. 9 (8), 3883–3898.
Pepe, A., Bonano, M., Zhao, Q., Yang, T., Wang, H., 2016b. The use of C-/X-band time-gapped SAR data and geotechnical models for the study of Shanghai's ocean-reclaimed lands through the SBAS-DInSAR technique. Remote Sensing 8 (11), 911.
Pfeffer, W.T., Harper, J.T., O'Neel, S., 2008. Kinematic constraints on glacier contributions to 21st-century sea-level rise. Science 321 (5894), 1340–1343.
Ritz, C., Edwards, T.L., Durand, G., Payne, A.J., Peyaud, V., Hindmarsh, R.C.A., 2015. Potential sea-level rise from Antarctic ice-sheet instability constrained by observations. Nature 528, 115–118.
Sampson, C.C., Smith, A.M., Bates, P.D., Neal, J.C., Lorenzo, A., Freer, J.E., 2015. A high-resolution global flood hazard model. Water Resour. Res. 51 (9), 7358–7381.
Samsonov, S., d'Oreye, S., 2012. Multidimensional time-series analysis of ground deformation from multiple InSAR data sets applied to Virunga Volcanic Province. Geophys. J. Int. 191, 1095–1108.
State Oceanic Administration of People's Republic of China, 2008. China sea level bulletin 2007 (in Chinese).
State Oceanic Administration of People's Republic of China, 2017. China sea level bulletin 2016 (in Chinese).
Syvitski, J.P.M., Kettner, A.J., Overeem, I., Hutton, E.W.H., Hannon, M.T., Brakenridge, G.R., 2009. Sinking deltas due to human activities. Nat. Geosci. 2 (10), 681–686.
Tachikawa, T., Hato, M., Kaku, M., Iwasaki, A., 2011. Characteristics of ASTER GDEM version 2. In: Geoscience and Remote Sensing Symposium (IGARSS), 2011 IEEE International, IEEE, pp. 3657–3660.
Teatini, P., Tosi, L., Strozzi, T., 2011. Quantitative evidence that compaction of Holocene sediments drives the present land subsidence of the Po Delta, Italy. J. Geophys. Res. Solid Earth 116 (B8), 407–416.
Tian, B., Wu, W.T., Yang, Z.Q., Zhou, Y.X., 2016. Drivers, trends, and potential impacts of long-term coastal reclamation in China from 1985 to 2010. Estuar. Coast. Shelf Sci. 170, 83–90.
Usai, S., 2003. A least squares database approach for SAR interferometric data. IEEE Trans. Geosci. Remote Sens. 41 (4), 753–760.
Vaughan, D.G., Spouge, J.R., 2002. Risk estimation of collapse of the west Antarctic ice sheet. Clim. Change 52 (1–2), 65–91.
Wang, J., Gao, W., Xu, S., Yu, L., 2012. Evaluation of the combined risk of sea level rise, land subsidence, and storm surges on the coastal areas of Shanghai, China. Clim. Change 115, 537–558.
Weigt, M., Rizzoli, P., Bachmann, M., Bräutigam, B., Schulze, D., 2012. TanDEM-X mission — interferometric performance and global DEM acquisition status. Radar 2012, IET International Conference on Radar Systems, Glasgow, UK, 22–25, Oct. 2012.
Wessel, P., Smith, W.H.F., Scharro, R., Luis, J.F., Wobbe, F., 2013. Generic Mapping Tools: Improved version released. EOS Trans. Am. Geophys. Union 94, 409–410.
Shi, Y., Zhu, J., Xie, Z., Ji, Z., Jiang, Z., Yang, G., 2012. Prediction and prevention of the impacts of sea level rise on the Yangtze River Delta and its adjacent areas. Sci. China, Ser. D Earth Sci. 43, 412–422.
Yang, L., Meng, X., Zhang, X., 2011a. SRTM DEM and its application advances. Int. J. Remote Sens. 32 (14), 3875–3896.
Yang, S., Milliman, J.D., Li, P., Xu, K., 2011b. 50,000 dams later: Erosion of the Yangtze River and its delta. Global Planetary Change 75, 14–20.
Yang, Y.-Q., Tang, N.-Q. Zhou, Wang, J.-X., 2008. Consolidation settlement of Shanghai dredger fill under self-weight using centrifuge modeling test. J. Cent. South Univ. Technol. 39 (4), 862–866 (in Chinese).
Yin, J., Yu, D., Yin, Z., 2016a. Evaluating the impact and risk of pluvial flash flood on intra-urban road network: a case study in the city center of Shanghai, China. J. Hydrol. 537, 138–145.
Yin, J., Lin, N., Yu, D., 2016b. Coupled modeling of storm surge and coastal inundation: a case study in New York City during Hurricane Sandy. Water Resour. Res. 52, 8685–8699.
Yin, J., Yu, D., Yin, Z., Wang, J., Xu, S., 2013. Modeling the combined impacts of sea-level rise and land subsidence on storm tides induced flooding of the Huangpu River in Shanghai. China. Climatic Change 119 (3), 919–932.
Yu, D., Lane, S.N., 2006a. Urban fluvial flood modeling using a two-dimensional diffusion wave treatment, part 1: mesh resolution effects. Hydrol. Process. 20, 1541–1565.
Yu, D., Lane, S.N., 2006b. Urban fluvial flood modeling using a two-dimensional diffusion wave treatment, part 2: development of a sub grid-scale treatment. Hydrol. Process. 20, 1567–1583.
Yu, D., Lane, S.N., 2011. Interaction between subgrid-scale resolution, feature representation and grid-scale resolution in flood inundation modeling. Hydrol. Process. 25, 36–53.
Yu, L., Yang, T., Zhao, Q., Liu, M., Pepe, A., 2017. The 2015–2016 ground displacements of the Shanghai Coastal area inferred from a combined COSMO-SkyMed/Sentinel-1 DInSAR analysis. Remote Sens. 9, 1194.
Zhao, Q., Pepe, A., Gao, W., Lu, Z., Bonano, M., He, M., Wang, J., Tang, X., 2015. A DInSAR investigation of the ground settlement time evolution of ocean-reclaimed lands in Shanghai. IEEE J. Sel. Top. Appl. Earth Obs. Remote Sens. 8 (4), 1763–1781.